COMMUNICATIONS CHEMISTRY

ARTICLE

https://doi.org/10.1038/s42004-019-0223-3 OPEN

Voltage fade mitigation in the cationic dominant lithium-rich NCM cathode

Prem Chandan[1,7], Chung-Chieh Chang[2,7], Kuo-Wei Yeh[2], Chui-Chang Chiu[2], Dong-Ze Wu[1], Tzu-Wen Huang[1], Phillip M. Wu[1], Po-Wei Chi[1], Wei-Fan Hsu[1], Kai-Han Su[3], Yu-Wen Lee[4], Hua-Shu Chang[1], Ming-Jye Wang[5], Heng-Liang Wu[4], Horng-Yi Tang[6*] & Maw-Kuen Wu[1*]

In the archetypal lithium-rich cathode compound $Li_{1.2}Ni_{0.13}Co_{0.13}Mn_{0.54}O_2$, a major part of the capacity is contributed from the anionic ($O^{2-/-}$) reversible redox couple and is accompanied by the transition metal ions migration with a detrimental voltage fade. A better understanding of these mutual interactions demands for a new model that helps to unfold the occurrences of voltage fade in lithium-rich system. Here we present an alternative approach, a cationic reaction dominated lithium-rich material $Li_{1.083}Ni_{0.333}Co_{0.083}Mn_{0.5}O_2$, with reduced lithium content to modify the initial band structure, hence ~80% and ~20% of capacity are contributed by cationic and anionic redox couples, individually. A 400 cycle test with 85% capacity retention depicts the capacity loss mainly arises from the metal ions dissolution. The voltage fade usually from Mn^{4+}/Mn^{3+} and/or O^{n-}/O^{2-} reduction at around 2.5/3.0 V seen in the typical lithium-rich materials is completely eliminated in the cationic dominated cathode material.

[1] Institute of Physics, Academia Sinica, Taipei, Taiwan 11529. [2] Gus Technology Co. Ltd., New Taipei City, Taiwan 22175. [3] Institute of Mechatronic Engineering, National Taipei University of Technology, Taipei, Taiwan 10608. [4] Center for Condensed Matter Sciences, National Taiwan University, Taipei, Taiwan 10617. [5] Institute of Astronomy and Astrophysics, Academia Sinica, Taipei, Taiwan 11529. [6] Department of Applied Chemistry, National Chi Nan University, Puli, Taiwan 545. [7] These authors contributed equally: Prem Chandan, Chung-Chieh Chang. *email: hytang@ncnu.edu.tw; mkwu@phys.sinica.edu.tw

Fast charging, lightweight and stable storage techniques can complement the green energy generation sources such as wind or solar to provide efficient and completely renewable energy systems. Scientists have been incessantly working on developing various lithium-based compounds such as high nickel NCM811 and NCA to meet the needs[1–9]. However, from their intrinsic layered-type structure, these compounds have limited specific capacity by the number of lithium ions that can participate in redox reactions. Over-delithiation accompanied by the high oxidation state of transition metal gradually destabilizes the layered structure resulting in lattice collapse[10,11].

About a decade ago, a new concept of "lithium-rich" materials, with the chemical formula $xLi_2MnO_{3\cdot(1-x)}LiMO_2$ or $Li(Li_wNi_xCo_yMn_z)O_2$, was introduced by Thackeray. The "Mn-based" compounds have excess lithium to provide high specific capacity[12,13]. Many different ternary transition metal compounds and their rich structure phase diagram have been reported[14–17]. Dahn's group completed a pseudo-quaternary phase diagram using automatic combinatorial synthesis[18]. A substantial number of compositions, nearly 800, with layered or spinel structure have been clearly identified[3]. Due to ions migration leads to an unusual atomic restructuring hence most phases are even more complicated after the first cycle[19–22].

Despite the versatile elemental combination and structural complexity, it is recognized that the high capacity of Li-rich Mn-based compound accounts from both cationic and anionic redox couples[23]. For instance, a well-studied material, $Li_{1.2}Ni^{2+}_{0.13}Co^{3+}_{0.13}Mn^{4+}_{0.54}O_2$ has been reported to exhibit redox activity both on the transition metals and on oxygen, and the capacity from cationic redox couples ($Ni^{2+/4+}$, $Co^{3+/4+}$) is ~122 $mAhg^{-1}$ while anionic redox couple ($O^{2-/-}$) contributes more than 50% of the capacity depending on the end of charging potential[23–28]. The major part of capacity arises from high voltage anionic redox reaction and occurs simultaneously with defects formation and ions migration. The valence states of transition metals and oxygen above 4.5 V vs. Li, studied by soft X-ray absorption spectroscopy (SXAS) and resonant inelastic X-ray scattering spectroscopy, have been identified as Ni^{4+}, Co^{4+}, Mn^{4+} and O^{n-} $(1 \le n \le 2)$[27]. Theoretical calculation and experimental observations propose a specific honeycomb-like short-range ordering of Mn^{4+}, Li^{+}, and O^{n-} that benefits the structure stability and activates anionic redox couple[27,28]. Nevertheless, despite these Li-rich compounds display a high capacity, they have not yet been fully commercialized.

To improve the cycling stability of these cathode materials, fundamental problems of the gradual irreversible phase transformation and detrimental voltage fade at around 2.5/3.3 V must be solved before getting into the real application. However, several debates about the evolution of voltage fade exist in the literature[29–33]. Many reported Li-rich Mn-based compounds display different capacity hysteresis between 1st and 2nd cycle at around 2.5/3.3 V where it is considered to undergo an irreversible phase transformation from its initial state to spinel-like phase[17,32]. Cheuh et al. proposed the coupling effects for cation migration and oxygen redox reaction[31]. A drastic change at around 2.5/3.3 V in the 2nd cycle of dQ/dV curve corresponds to the cations migration associated with the electronic reshuffling involving oxygen redox reaction[34]. Based on the theoretical band structure studies, the *d-d* Coulomb interaction (U) resulting in different M-O* peak splitting and overlapping with O 2*p* non-bonding band, Tarascon proposed three cationic/anionic redox reaction scenarios based on different ratios of U and charge transfer energy Δ[23].

Since different experimental results are shown in these studies, the development of various stable Li-rich Mn-based compounds will benefit the fundamental research on the complex voltage fade issue. In an attempt to find a different initial band structure material, we designed a cationic dominated Li-rich Mn-based cathode material $Li_{1.083}Ni_{0.333}Co_{0.083}Mn_{0.5}O_2$, formulated as Li$(Li^{+}_{1/12}Ni^{2+}_{1/3}Co^{3+}_{1/12}Mn^{4+}_{1/2})O_2$ and abbreviated as (LNCM1416) after reduction to common denominator, which has a single-phase monoclinic structure of *C*2/*m* symmetry identified by Rietveld refinement of synchrotron X-ray diffraction (XRD), high-resolution transmission electron microscopy (HR-TEM) and selected area electron diffraction (SAED). We have also examined the magnetic responses of the materials after discharged to the certain specific voltages as measured by SQUID (superconducting quantum interference device)[34,35]. The oxygen oxidation reaction of LNCM1416 material is initiated at 4.4 V, wherein the capacity is achieved from around 20% anionic and 80% cationic redox couples. Since no reduction of oxygen species is observed at lower voltages and the compound has a reversible oxygen redox reaction at above 4.4 V, possibly it can be placed in the second case of cathode materials with $U/2 \approx \Delta$ as mentioned by Tarascon[23]. No significant voltage fade at around 3.0/3.3 V in the initial 100 cycles, unlike $Li_{1.2}Ni_{0.13}Co_{0.13}Mn_{0.54}O_2$ reflects a much more stable charge/discharge process of LNCM1416 material. However, the gradual decay in capacity along 400 cycles is due to the dynamic voltage separation of transition metal redox couple or the dissolution and redeposition of metal ions on the anode surface.

In this work, we demonstrate the potential real application of cationic Li-rich Mn-based material via 60 mAh full cell with 205 $mAhg^{-1}$ capacity with 85% retention after 400 cycles displaying minimal voltage fade at lower voltages and reversible redox reaction of oxygen at the higher voltages.

Results

Synthesis and structure characterization of LNCM1416 cathode material. The synthesized Li-rich phase highly depends on the controlled atmosphere as well as the temperature profile used. To optimize the quaternary LNCM1416 material, the sample prepared with an excess of 2 mol% Li_2CO_3 and heating with the flow of oxygen are absolutely necessary. Figure 1 displays the synchrotron XRD pattern of the pristine LNCM1416 cathode

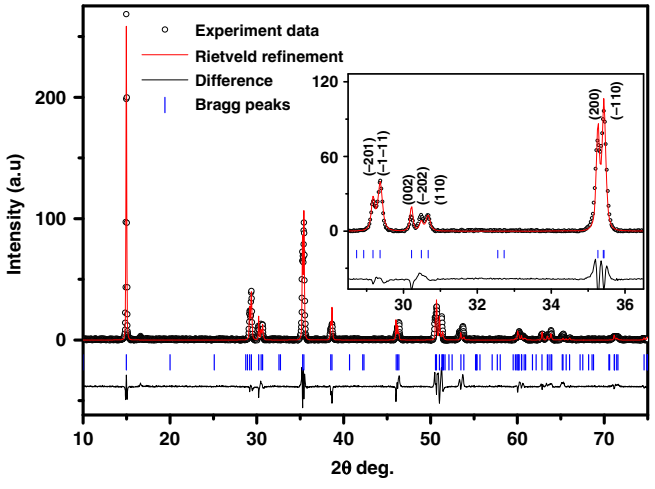

Fig. 1 The synchrotron XRD pattern (circle) and the simulated pattern of *C*2/*m* symmetry (red line) of LNCM1416. $R\bar{3}m$ space group with 0.35% extension of γ angle along the *a*-axis direction was used for achieving the single-phase fitting of LNCM1416. The monoclinic lattice with higher symmetry can be cleaved and subscribed from this distorted $R\bar{3}m$ structure, hence, showing a single-phase structure with monoclinic *m*-$LiMnO_2$ (*C*2/*m*) space group

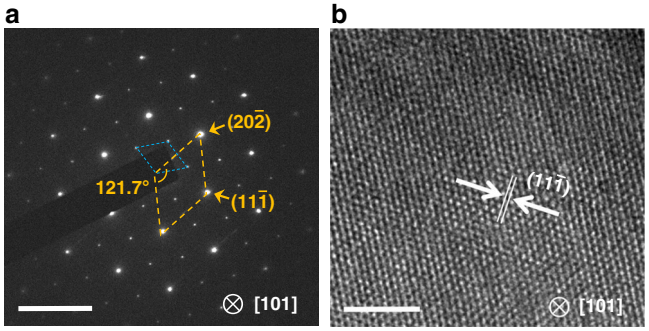

Fig. 2 Confirmation of single phase of LNCM1416 with *C*2/*m* symmetry. **a** SAED pattern taken along [101] zone axis indexed with respect to the monoclinic *C*2/*m* symmetry verifies the single phase of LNCM1416. **b** HR-TEM image of LNCM1416 sample shows the lattice fringes reflecting the crystalline nature of the material corresponding to the (11$\bar{1}$) crystal plane. Scale bar: **a** 5 nm^{-1}, **b** 5 nm

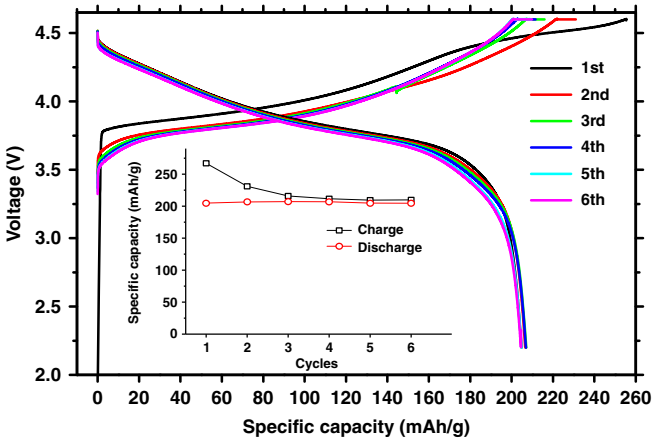

Fig. 3 Voltage vs. specific capacity of LNCM1416 coin cell. The first six cycles of 0.1 C charge/discharge run in the voltage range of 2.2–4.6 V shows the specific capacity of about 205 $mAhg^{-1}$

material. The attempt to refine the data using the $R\bar{3}m$ structure of $LiMnO_2$ resulted in a bad fitting with high R_{wp}. Thus, a combinatorial data mining approach was applied to search for the possibility of lattice distortion. The best-fitting result gave a lattice compression angle of 120.417 ± 0.043° along the *a*-axis of hexagonal lithium lattice plane and the splitting fitted well with a satisfactorily low R_{wp} (<15%) as shown in the inset of Fig. 1. Therefore, the single-phase fitting of LNCM1416 can be achieved using $R\bar{3}m$ space group but with 0.35% extension of γ angle along the *a*-axis direction. The monoclinic lattice with higher symmetry can be cleaved and subscribed from this distorted $R\bar{3}m$ structure, hence, showing a single-phase structure with monoclinic *m*-$LiMnO_2$ (*C*2/*m*) space group, as seen in Fig. 2b. The obtained lattice parameters are $a = 4.9997$ Å, $b = 2.8602$ Å, $c = 5.8086$ Å, $\alpha = \gamma = 90°$, $\beta = 125.0179°$.

The fine structures of Li-rich $Li_{1.2}Ni_{0.13}Co_{0.13}Mn_{0.54}O_2$ compound, either a *C*2/*m* single phase or an intermixed of layered $LiMO_2$ with monoclinic Li_2MnO_3 two phases, have been discussed for a long time[11,36]. HR-TEM and SAED confirm the single phase of LNCM1416 with *C*2/*m* structure from reciprocal space images taken along [101] zone axis as shown in Fig. 2a. The diffraction pattern can be indexed with respect to a typical *C*2/*m* space group and the reciprocal lattice is in good agreement with synchrotron XRD result seen in Fig. 1. The cathode material LNCM1416 with *C*2/*m* symmetry, which we have designed, its chemical stoichiometry falls into Dahn's published phase diagram at the layered and spinel structure boundary[18]. Sample preparation without precise Li stoichiometry control may result in the $R\bar{3}m$ symmetry product, which in turn is unable to achieve a high capacity as obtained from the *C*2/*m* distorted structure.

Electrochemical studies and evolution of voltage fade. For the material's electrochemical studies, charge/discharge tests were carried out in order to investigate the maximum capacity attainable from the material and retention of its structural stability after many cycles. Initially, coin cells were prepared with lithium metal disc as anode for running the preliminary tests. The coin cells were charged up to 4.6 V and discharged to 2.2 V in CC/CV mode. A discharge specific capacity of 205 $mAhg^{-1}$ was obtained with good consistency in the first six cycles as seen in Fig. 3. From the charge curves, it is clear that $O^{2-/-}$ redox couples occurred at above 4.4 V and from the deduction, ~20% of the capacity is acquired from the anionic redox reaction, and consequently; ~80% capacity attained is from cationic redox couples.

Significant lithium movement in the layered cathode materials normally can lead to structural instability. Cyclic voltammetry (CV) and differential capacity d*Q*/d*V* studies of LNCM1416 material show ions migration occurred at high voltage and formed a dynamic structure in each cycle.

Cyclic voltammetry of coin cell was carried out by five continuous scans at the scan rate of 0.1 mV/s in the potential range 2.2–4.5 V as shown in Fig. 4a. The 1st CV scan of as-prepared LNCM1416 coin cell reveals two anodic reactions that denote the oxidation of ($Ni^{2+/4+}$, $Co^{3+/4+}$) and O^{2-}/O^{1-} separately. The difference found in the 2nd cycle is at high voltage oxidation process. In the 1st cycle, the second oxidation peak begins at around 4.4 V but disappeared on the 2nd cycle. The disappearance of O^{2-}/O^{1-} signal and poor initial coulombic efficiency (Fig. 3 inset) indicate the possible generation of vacancy in oxygen layer and/or redistribution of metal cations, resulting in an irreversible lattice transformation, which may cope with the distorted structure, intrinsic to the LNCM1416 material so that the following CV cycles become stable.

By differential capacity analysis, d*Q*/d*V* plots of LNCM1416 coin cell in Fig. 4b show the 2nd discharge profile nearly overlapped with the 1st cycle, but display a shifting towards lower voltage during initial 20 cycles, and becomes pronounced voltage fade at around 2.5/3.3 V after 100 cycles. Contrarily, in the reported compound $Li_{1.2}Ni_{0.13}Co_{0.13}Mn_{0.54}O_2$, the voltage fade at 2.5/3.3 V can be observed immediately after few cycles where it is considered to undergo an irreversible atomic restructuring accompanied with dynamic electronic reshuffling to generate such voltage fade. Although the evolution of voltage fade for LNCM1416 material is much slower than $Li_{1.2}Ni_{0.13}Co_{0.13}Mn_{0.54}O_2$ compound, a clear voltage fade at 100th cycle can be seen. In the coin cell long cycles experiment, lack of activation steps involving the removal of side products could result in undesired reactions such as the serious dissolution of metal ions and electrolyte decomposition at high voltage.

In Fig. 4c, a 60 mAh pouch cell was made by the same batch of LNCM1416 material for parallel charge/discharge cycling test, assembled with carbon-based anode activated and tested in the voltage range 2.2–4.5 V. Its 100th cycle discharge profile has an insignificant voltage fade at around 2.5/3.0 V (green area). The pouch cell results demonstrate the voltage fade in LNCM1416 material can be effectively reduced by proper activation steps that include the removal of gases produced from the side reactions. After 400 cycles, in d*Q*/d*V* plots, a noticeable voltage separation of transition metals redox couples around 3.0/3.5 V (pink area) is

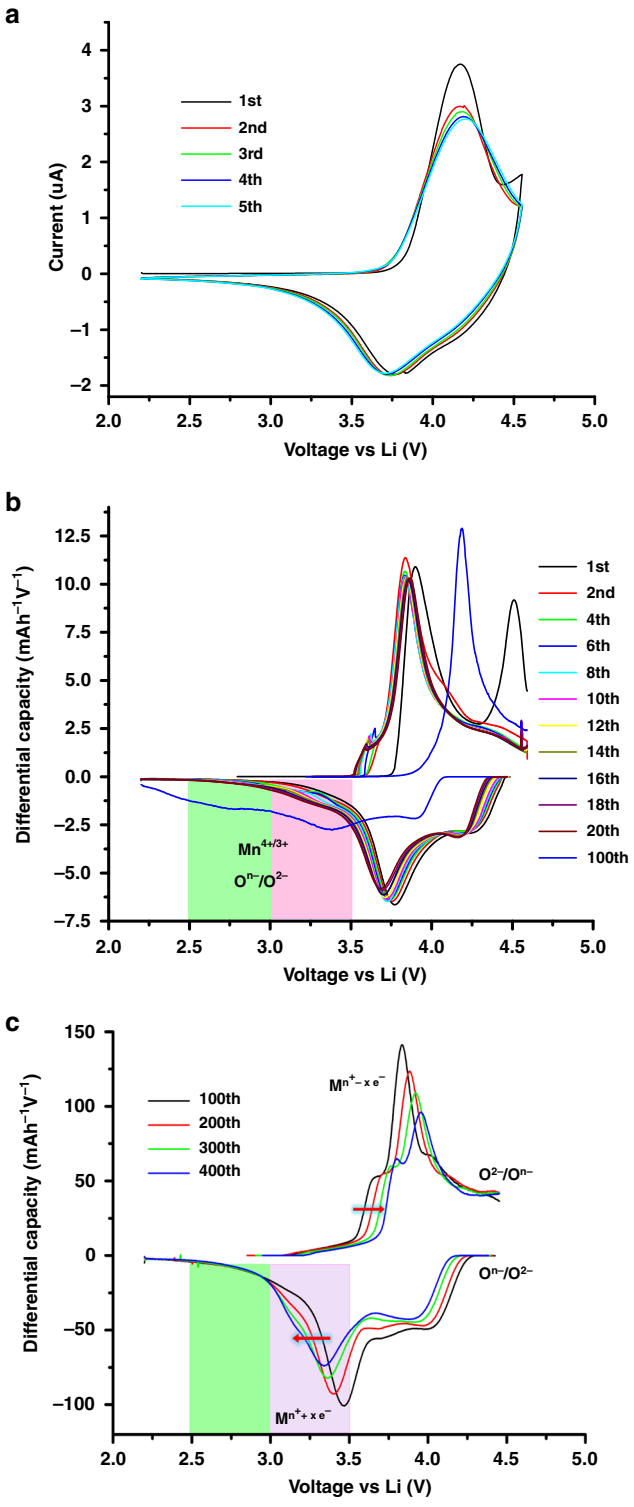

Fig. 4 Electrochemical analysis of LNCM1416. **a** The first five continuous CV scans of LNCM1416 cathode at the scan rate of 0.1 mVs^{-1} in the potential range of 2.2–4.5 V displays the irreversible behavior in the first cycle that is caused due to the oxidation reaction of O^{2-}/O^{1-} initiated at 4.4 V which disappears in the later cycles. **b** The d*Q*/d*V* plots of first 100 cycles run with the coin cell at 0.1 C rate portrays the gradual appearance of voltage fade at lower voltage which possibly instigated from the lack of activation steps involving the removal of the side products. **c** The d*Q*/d*V* plots of pouch cell of 60 mAh run at 0.2 C rate for 400 cycles in the potential range of 2.2–4.5 V, shown with the 100 cycles/increment, clearly demonstrates that with proper activation stop, the voltage fade at lower voltage can be effectively suppressed. A noticeable voltage separation of transition metals redox couples around 3.0/3.5 V (pink area), however, can be observed, which is highly correlated to the capacity fade mechanism resulting from the metal ions dissolution, dynamic structure formation, and redeposition on the anode surface

observed in the pouch cell, which is highly correlated to the capacity fade mechanism resulting from the metal ions dissolution, dynamic structure formation and redeposition on the anode surface. More specifically, only redox potentials separation can be observed but no detectable new redox couple is developed at around 2.5/3.5 V. The LNCM1416 cathode material sustains at 4.5 V for 400 cycles and no detectable macroscopic spinel-like phase formation is observed as seen in the ex situ XRD data presented in the Supplementary Fig. 1, showing its monoclinic *C*2/*m* structure is thermodynamically stable and suggests the oxygen redox couple at high voltage is reversible. Also, from the SEM-EDX studies of the post-electrochemical LNCM1416 cathode as shown in the Supplementary Fig. 2, it is evident that the cathode material is stoichiometrically intact even after 400 cycles.

To test the efficiency of the cells along with its structural stability at higher current rates, the cells were discharged at various discharge rates starting from 0.2 to 5 C. A noticeable discharge capacity was attained at the lower C-rates, i.e., 193, 178, and 158 mAhg^{-1} at 0.2, 0.5, and 1 C, respectively, which decreased drastically when increased to 3 C and 5 C rates with the discharge capacity of 130 and 84 mAhg^{-1} as seen in Fig. 5a. However, the recovery of the cells back to 200 mAhg^{-1} at 0.1 C after the high C-rate tests is significant, reflecting the structural stability of the active material. A 60 mAh pouch cell tests, in the voltage range 2.2–4.5 V as shown in Fig. 5b, displays 200 mAh/g initial capacity and 85% retained after 400 cycles in 0.2 C charge/discharge rate. The initial rise in the capacity up to 50 cycles is due to the lower charging voltage of 4.5 V that progressively activates the oxygen redox couple, which otherwise would be flat when charged to 4.6 V as seen in Fig. 3.

SQUID and operando XRD measurements. To analyze the LNCM1416 valence state variation during the charge/discharge process, samples discharged to a selected potential were opened and packed in the glove box for SQUID measurement. Figure 6a displays the temperature-dependent inverse susceptibility ($1/\chi$) for the samples after discharged to specified voltages. We observed that the magnetic susceptibility falls into two groups with different temperature dependence. The samples after charged above 4.25 V show paramagnetic behavior. The calculated experimental effective moment for sample discharge at 4.55 V is $\mu_{eff} \sim 2.069\,\mu_B$ (Bohr magneton), which fits well by the formula $Li_{0.32}Ni_{0.34}Co_{0.08}Mn_{0.5}O_2$ with Mn^{4+}, Ni^{4+} & Co^{4+} oxidation states. The experimental effective moment for sample after discharged at 4.25 V, $\mu_{eff} \sim 2.166\,\mu_B$, corresponding to the stoichiometry of $Li_{0.456}Ni^{3+}{}_{0.136}Ni^{4+}{}_{0.204}Co^{4+}{}_{0.08}Mn^{4+}{}_{0.5}O_2$. The effective moment for 4.5 V sample is also within the error range.

It was a surprise to observe the rise in susceptibility below ~180 K for samples discharged at 3 V and ~150 K at 3.75 V, respectively, suggesting a magnetically more ordered state at low temperature in these samples. The effective moments of these two samples, estimated from the high temperature data, are closer to that of the 4.25 V sample. This observation seems to be consistent with the operando XRD results, as shown in Fig. 6b, which exhibit the reduction in c-lattice at the same discharging voltages. The c-lattice contraction enhanced the coupling between magnetic ions

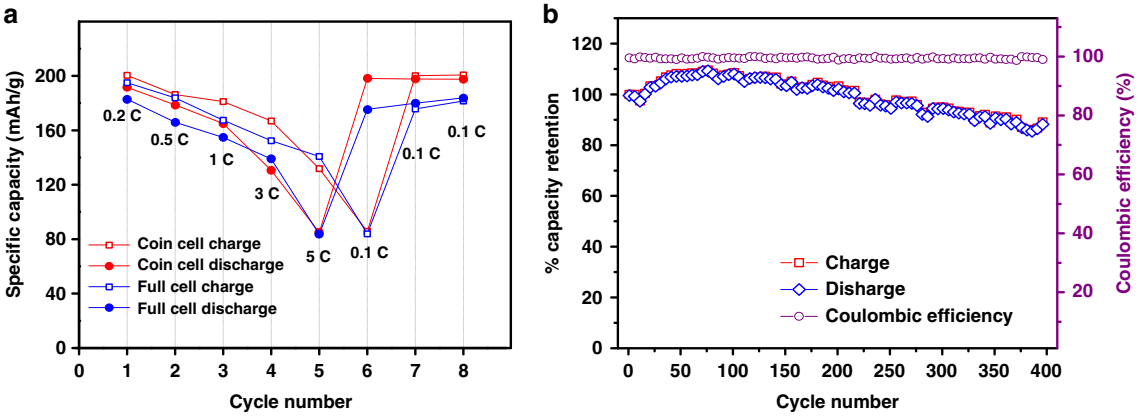

Fig. 5 Efficiency test of the LNCM1416 material. **a** C-rate test of cells carried out with various discharge rates starting from 0.2 to 5 C while maintaining the charging rate at 0.1 C in the potential range 2.2–4.5 V. **b** Cyclability was tested with the pouch cell in the voltage range 2.2–4.5 V. A considerable discharge specific capacity of ~200 $mAhg^{-1}$ was observed with the capacity decay of around 15% after 400 cycles of charge/discharge

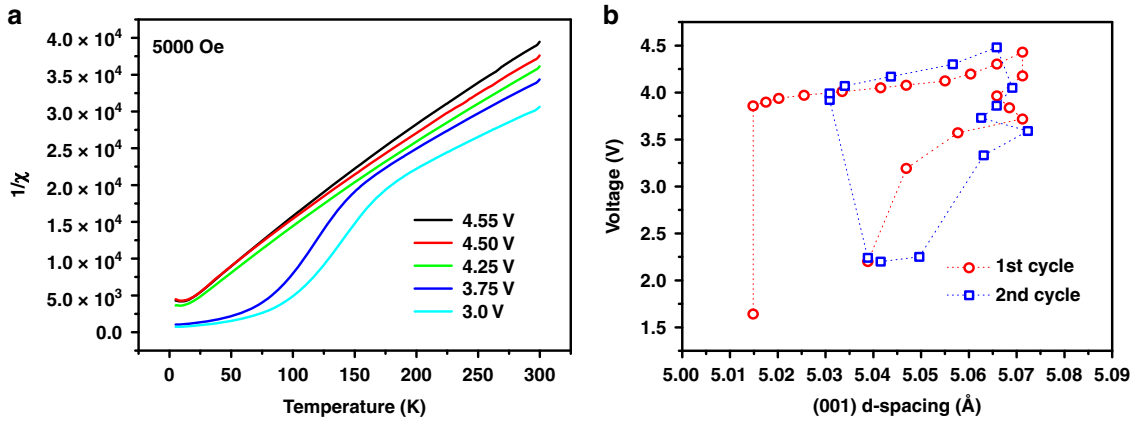

Fig. 6 Understanding the chemical variation of LNCM1416 during the charge/discharge. **a** SQUID measurement of LNCM1416 displays the temperature-dependent inverse susceptibility at the applied field of 5000 Oe after discharging to 3.0, 3.75, 4.25, 4.5, and 4.55 voltages. **b** d-spacing versus voltage, displaying the variation of (001) interplanar spacing along the two cycles of charge/discharge, calculated from the operando XRD studies presented in the Supplementary Fig. 3

to make it magnetically more ordered at low temperature. Therefore, similar to α-$NaMnO_2$ and $CuMnO_2$, the monoclinic distortion in LNCM1416 results from the strong cooperative effect on ionic size difference and specific spin alignment.

Discussion

A systematic study on the designed cationic Li-rich compound LNCM1416 was carried out that demonstrated the detrimental voltage fade at low voltage can be effectively suppressed. Not taking into account the voltage fade issue, the 15% capacity loss after 400 cycles of charge/discharge in the full cell depicts the voltage separation of transition metal redox couple is the major factor for cell degradation. LNCM1416 material is comparable to the commercially available material NCM811 in terms of capacity. Nevertheless, more Mn with less Ni in LNCM1416 certainly has the advantage of a substantial reduction in cost. In this work, we have further demonstrated the potential real application of cationic Li-rich Mn-based material via 60 mAh full cell with 205 $mAhg^{-1}$ capacity and 85% retained after 400 cycles.

Methods

Preparation of electrode materials. The cathode material LNCM1416 was synthesized using a co-precipitation method. 1000 ml of the aqueous solution of transition metal nitrates (0.34 M $Ni(NO_3)_2$, 0.5 M $Mn(NO_3)_2$, 0.08 M $Co(NO_3)_2$), and 1000 ml of 2 M LiOH aqueous solution were dripped simultaneously into a five-liter reactor using a peristaltic pump and stirred continuously at 700 rpm for 12 h. The reactor was constantly maintained in the nitrogen atmosphere to avoid undesirable side reactions. The precipitate was collected, filtered and washed with DI water, and then dried overnight at 110 °C in the oven. The dried precipitate was further ball-milled with Li_2CO_3 and then heated under oxygen gas flow at 900 °C for 10 h with a ramp of 5 °C/min to finally obtain the spherical shaped stoichiometric LNCM1416 cathode material.

Cell preparation and electrochemical measurements. Composite electrodes were prepared with 91 wt% active material, 5 wt% polyvinylidene fluoride (Kureha Chemical), 2 wt% carbon black (Denka, 50% compressed), and 2 wt% KS-6 synthetic graphite (Timcal, Graphites and Technologies) in N-methyl-2-pyrrolidinone (NMP) and cast onto aluminum foil current collectors with typical active material loadings of 6–7 mg/cm^2. For this study, CR-2032 coin cells were assembled in an argon-filled glove box using the composite electrode as the positive electrode and Li metal as the negative electrode. A Foresight 20-μm pp separator and 1.0 M $LiPF_6$ electrolyte solution in 55% diethyl carbonate (DEC):35% ethylene carbonate (EC):5% propylene carbonate (PC):3% fluoroethylene carbonate (FEC):2% vinylene carbonate (VC) w/w were used to fabricate the coin cells. Carbon-based material coated on a 10-μm-thick copper foil was used as the anode in the case of full cell while the rest were similar as in the coin cells. Battery testing was performed on a computer-controlled potentiostat/galvanostat (ThinkLab battery test system). C-rate of 1 C was defined as fully charging a cathode in 1 h, corresponding to a specific current density of 205 mAg^{-1}. The electrodes were removed from coin cells, rinsed with dimethyl carbonate and dried in an Argon-filled glove box for

further study. For electron microscopy and spectroscopy measurements, the electrode particles were scratched off and deposited onto the respective substrates. A hole of 3 mm diameter was made in all the components except for the cathode, to avoid any unfavorable signals and both the ends were sealed with Kapton film for operando XRD measurements.

Materials characterization. X-ray diffraction (XRD) on powder samples was performed on a Bruker D2 Phaser diffractometer using CuK_α radiation. Precise cell parameters were refined from the experiments performed in synchrotron source (TPS-09A at NSRRC) with an incident beam of wavelength 0.82656 Å. Operando XRD measurements were carried out by using beam-line #01C2 of Taiwan Light Source, NSRRC in Taiwan. The wavelength of incident X-ray is 0.77491 Å (16 keV). JEOL high-resolution transition electron microscope (HR-TEM) operated at 200 kV was used for microstructural analysis. The magnetic properties were measured on a SQUID magnetometer (MPMS, Quantum Design Inc.) starting from 0 to 300 K.

Data availability

The data supporting the findings of this study are available within the article and its Supplementary Information files. All other relevant source data are available from the corresponding authors upon reasonable request.

Received: 6 June 2019; Accepted: 25 September 2019;
Published online: 24 October 2019

References

1. Ohzuku, T. & Makimura, Y. Layered lithium insertion material of $LiCo_{1/3}Ni_{1/3}Mn_{1/3}O_2$ for lithium-ion batteries. *Chem. Lett.* **30**, 642–643 (2001).
2. Kang, K., Meng, Y. S., Bréger, J., Grey, C. P. & Ceder, G. Electrodes with high power and high capacity for rechargeable lithium batteries. *Science* **311**, 977–980 (2001).
3. Kwak, W. J., Park, N. Y. & Sun, Y. K. ICAC 2018: The First International Conference focused on NCM & NCA cathode materials for lithium ion batteries. *ACS Energy Lett.* **3**, 2757–2760 (2018).
4. Qiu, L. et al. Polyanion and cation co-doping stabilized Ni-rich Ni–Co–Al material as cathode with enhanced electrochemical performance for Li-ion battery. *Nano Energy* **63**, 103818 (2019).
5. Li, Y.-C. et al. Construction of homogeneously Al^{3+} doped Ni-rich Ni-Co-Mn cathode with high stable cycling performance and storage stability via scalable continuous precipitation. *Electrochim. Acta* **291**, 84–94 (2018).
6. Xu, Y.-D. et al. Improving cycling performance and rate capability of Ni-rich $LiNi_{0.8}Co_{0.1}Mn_{0.1}O_2$ cathode materials by $Li_4Ti_5O_{12}$ coating. *Electrochim. Acta* **268**, 358–364 (2018).
7. Sohn, H. et al. Porous spherical carbon/sulfur nanocomposites by aerosol-assisted synthesis: the effect of pore structure and morphology on their electrochemical performance as lithium/sulfur battery cathodes. *Appl. Mater. Interfaces* **6**, 7596–7606 (2014).
8. Sohn, H. et al. Porous spherical polyacrylonitrile-carbon nanocomposite with high loading of sulfur for lithium–sulfur batteries. *J. Power Sources* **302**, 70–78 (2016).
9. Xu, C. et al. Highly stabilized ni-rich cathode material with mo induced epitaxially grown nanostructured hybrid surface for high-performance lithium-ion batteries. *ACS Appl. Mater. Interfaces* **11**, 16629–16638 (2019).
10. Lin, F. et al. Surface reconstruction and chemical evolution of stoichiometric layered cathode materials for lithium-ion batteries. *Nat. Commun.* **5**, 3529 (2014).
11. Shukla, A. K. et al. Unravelling structural ambiguities in lithium- and manganese-rich transition metal oxides. *Nat. Commun.* **6**, 8711 (2015).
12. Thackeray, M. M. et al. Li_2MnO_3-stabilized $LiMO_2$ (M = Mn, Ni, Co) electrodes for lithium-ion batteries. *J. Mater. Chem.* **17**, 3112–3125 (2007).
13. Johnson, C. S., Li, N. C., Lefief, C., Vaughey, J. T. & Thackeray, M. M. Synthesis, characterization and electrochemistry of lithium battery electrodes: xLi_2MnO_3. $(1-x)LiMn_{0.333}Ni_{0.333}Co_{0.333}O_2$ $(0 < x < 0.7)$. *Chem. Mater.* **20**, 6095–6106 (2008).
14. Mohanty, D. et al. Investigating phase transformation in the $Li_{1.2}Co_{0.1}Mn_{0.55}Ni_{0.15}O_2$ lithium-ion battery cathode during high-voltage hold (4.5 V) *via* magnetic, X-ray diffraction and electron microscopy studies. *J. Mater. Chem. A* **1**, 6249–6261 (2013).
15. Ates, M. N., Mukerjee, S. & Abraham, K. M. A high rate Li-rich layered MNC cathode material for lithium-ion batteries. *RSC Adv.* **5**, 27375–27386 (2015).
16. Sarkar, T., Prakasha, K. R., Bharadwaj, M. D. & Prakash, A. S. Role of transition metals in a charge transfer mechanism and oxygen removal in $Li_{1.17}Ni_{0.17}Mn_{0.5}Co_{0.17}O_2$: experimental and first-principles analysis. *Phys. Chem. Chem. Phys.* **20**, 19606–19613 (2018).
17. Ishida, N., Tamura, N., Kitamura, N. & Idemoto, Y. Crystal and electronic structure analysis and thermodynamic stabilities for electrochemically or chemically delithiated $Li_{1.2-x}Mn_{0.54}Ni_{0.13}Co_{0.13}O_2$. *J. Power Sources* **319**, 255–261 (2016).
18. Brown, C. R., McCalla, E., Watson, C. & Dahn, J. R. Combinatorial study of the Li–Ni–Mn–Co oxide pseudoquaternary system for use in Li–ion battery materials research. *ACS Comb. Sci.* **17**, 381–391 (2015).
19. Benedek, R. First-cycle simulation for Li-rich layered oxide cathode material $xLi_2MnO_3{\cdot}(1-x)LiMO_2$ $(x = 0.4)$. *J. Electrochem. Soc.* **165**, A2667–A2674 (2018).
20. Croy, J. R. et al. Examining hysteresis in composite $xLi_2MnO_3{\cdot}(1-x)LiMO_2$ cathode structures. *J. Phys. Chem. C.* **117**, 6525–6536 (2013).
21. Bommel, A. V., Krause, L. J. & Dahn, J. R. Investigation of the irreversible capacity loss in the lithium-rich oxide $Li(Li_{1/5}Ni_{1/5}Mn_{3/5})O_2$. *J. Electrochem. Soc.* **158**, A731–A735 (2011).
22. Wang, J. et al. Lithium- and manganese-rich oxide cathode materials for high-energy lithium ion. *Batteries. Adv. Energy Mater.* **6**, 1600906 (2016).
23. Assat, G. & Tarascon, J. M. Fundamental understanding and practical challenges of anionic redox activity in Li-ion batteries. *Nat. Energy* **3**, 373–386 (2018).
24. Xie, Y., Saubanere, M. & Doublet, M. L. Requirements for reversible extra-capacity in Li-rich layered oxides for Li-ion batteries. *Energy Env. Sci.* **10**, 266–274 (2017).
25. Assat, G. et al. Fundamental interplay between anionic/cationic redox governing the kinetics and thermodynamics of lithium-rich cathodes. *Nat. Commun.* **8**, 2219 (2017).
26. Delmas, C. Operating through oxygen. *Nat. Chem.* **8**, 641–643 (2016).
27. Bruce, P. G. et al. Charge-compensation in 3d-transition-metaloxide intercalation cathodes through the generation of localized electron holes on oxygen. *Nat. Chem.* **8**, 684–691 (2016).
28. Seol, D. H. et al. The structural and chemical origin of the oxygen redox activity in layered and cation-disordered Li-excess cathode materials. *Nat. Chem.* **8**, 692–697 (2016).
29. Assat, G., Iadecola, A., Foix, D., Dedryvère, R. & Tarascon, J. M. Direct quantification of anionic redox over long cycling of Li-rich NMC via hard X-ray photoemission spectroscopy. *ACS Energy Lett.* **3**, 2721–2728 (2018).
30. Armstrong, A. R. et al. Demonstrating oxygen loss and associated structural reorganization in the lithium battery cathode $Li(Ni_{0.2}Li_{0.2}Mn_{0.6})O_2$. *J. Am. Chem. Soc.* **128**, 8694–8698 (2006).
31. Gent, W. E. et al. Coupling between oxygen redox and cation migration explains unusual electrochemistry in lithium-rich layered oxides. *Nat. Commun.* **8**, 2091 (2017).
32. Mohanty, D. et al. Unraveling the voltage fade mechanism in high-energy-density lithium-ion batteries: origin of the tetrahedral cations for spinel conversion. *Chem. Mater.* **26**, 6272–6280 (2014).
33. Myeong, S. et al. Understanding voltage decay in lithium-excess layered cathode materials through oxygen-centred structural arrangement. *Nat. Commun.* **9**, 3285 (2018).
34. Abdellahi, A., Urban, A., Dacek, S. & Ceder, G. The effect of cation disorder on the average Li intercalation voltage of transition-metal oxides. *Chem. Mater.* **28**, 3659–3665 (2016).
35. Klinser, G. et al. Charing processes in the cathode $LiNi_{0.6}Mn_{0.2}Co_{0.2}O_2$ as revealed by operando magnetometry. *J. Power Sources* **396**, 791–795 (2018).
36. Saubanere, M., McCalla, E., Tarascon, J. M. & Doublet, M. L. The intriguing question of anionic redox in high-energy density cathodes for Li-ion batteries. *Energy Env. Sci.* **9**, 984–991 (2016).

Acknowledgements

This research is supported by the Ministry of Science and Technology Grant MOST106-2633M-001-001, Academia Sinica Thematic Research Grant No. AS-TP-106-M01 and National Synchrotron Radiation Research Center, Taiwan.

Author contributions

P.C. and C.-C. Chang. contributed equally to this paper. P.C., C.-C. Chang., K.W.Y., C.-C. Chiu, and D.Z.W. designed and performed the experiments. T.W.H. and M.J.W. assisted in the extraction and the data analysis of XRD. P.W.C. and W.F.H. helped in running the SAED/HR-TEM experiments and analyzing the SAED data. K.H.S. and P.M.W. performed the SQUID and its data analysis. H.L.W. and Y.W.L. assisted in procuring and analyzing the operando XRD. H.S.C., H.Y.T., and M.K.W. supervised the project. P.C., H.Y.T., and M.K.W. prepared the paper. All the authors mentioned above were part of the discussion and provided their valuable inputs and comments on the paper.

Competing interests
The authors declare no competing interests.

Additional information
Supplementary information is available for this paper at https://doi.org/10.1038/s42004-019-0223-3.

Correspondence and requests for materials should be addressed to H.-Y.T. or M.-K.W.

Reprints and permission information is available at http://www.nature.com/reprints

Publisher's note Springer Nature remains neutral with regard to jurisdictional claims in published maps and institutional affiliations.